A Revised Conceptual Model of the Tropical Marine Boundary Layer. Part II: Detecting Relative Humidity Layers Using Bragg Scattering from S-Band Radar

JENNIFER L. DAVISON, ROBERT M. RAUBER, AND LARRY DI GIROLAMO

Department of Atmospheric Sciences, University of Illinois at Urbana–Champaign, Urbana, Illinois

(Manuscript received 26 November 2012, in final form 19 April 2013)

ABSTRACT

Persistent layers of enhanced equivalent radar reflectivity factor and reduced spectral width were commonly observed within cloud-free regions of the tropical marine boundary layer (TMBL) with the National Center for Atmospheric Research S-Pol radar during the Rain in Cumulus over the Ocean (RICO) field campaign. Bragg scattering is shown to be the primary source of these layers. Two mechanisms are proposed to explain the Bragg scattering layers (BSLs), the first involving turbulent mixing and the second involving detrainment and evaporation of cloudy air. These mechanisms imply that BSLs should exist in layers with tops (bases) defined by local relative humidity (RH) minima (maxima). The relationship between BSLs and RH is explored.

An equation for the vertical gradient of radio refractivity N is derived, and a scale analysis is used to demonstrate the close relationship between vertical RH and N gradients. This is tested using the derived radar BSL boundary altitudes, 131 surface-based soundings, and 34 sets of about six near-coincident, aircraft-released dropsondes. First, dropsonde data are used to quantify the finescale variability of the RH field. Then, within limits imposed by this variability, altitudes of tops (bases) of radar BSLs are shown to agree with altitudes of RH minima (maxima). These findings imply that S-band radars can be used to track the vertical profile of RH variations as a function of time and height, that the vertical RH profile of the TMBL is highly variable over horizontal scales as small as 60 km, and that BSLs are a persistent, coherent feature that delineate aspects of TMBL mesoscale structure.

1. Introduction

The trade wind environment is characterized by a high degree of moisture variability (e.g., Davison et al. 2013a, hereafter Part I). The vertical distribution of moisture has traditionally been measured with rawinsondes. Other instruments used to extract information about the moisture distribution include satellite imaging and sounding radiometers and interferometers, ground-based microwave radiometers and infrared interferometers, Raman and differential absorption lidars, and aircraft flight-level data. Radar refractivity has also been used to make measurements of near-surface moisture fields (e.g., Fabry et al. 1997; Roberts et al. 2008), and dual-wavelength radar observations have been used to produce water vapor density profile estimates (e.g., Ellis and Vivekanandan 2010).

During the Rain in Cumulus over the Ocean (RICO) experiment (Rauber et al. 2007), high-resolution S-band scanning radar observations, collected over the ocean from the remote Caribbean island of Barbuda, revealed persistent rings of enhanced equivalent radar reflectivity factor (hereafter reflectivity) and reduced spectral width (i.e., spectral width values well below values characteristic of noise) in cloud-free regions of the tropical marine boundary layer (TMBL) (Figs. 1a,b). The rings, a common feature throughout the 2-month-long RICO observational period, were often long lived, occurred in distinct layers, and were generally associated with cloud-free air (see radar geometry in Fig. 1c). This paper, the second in this series, explores the nature of these layers and their relationship to the vertical distribution of relative humidity (RH).

In this paper, we present evidence that the layers observed during RICO were caused by Bragg scattering. We then present an algorithm to derive the altitudes of the base and top of each Bragg scattering layer (BSL). Using these derived data, we demonstrate that the BSLs are persistent, coherent features of the TMBL that

Corresponding author address: Jennifer L. Davison, Department of Atmospheric Sciences, University of Illinois at Urbana–Champaign, 105 S. Gregory St., Urbana, IL 61801.
E-mail: jdavison@earth.uiuc.edu

DOI: 10.1175/JAS-D-12-0322.1

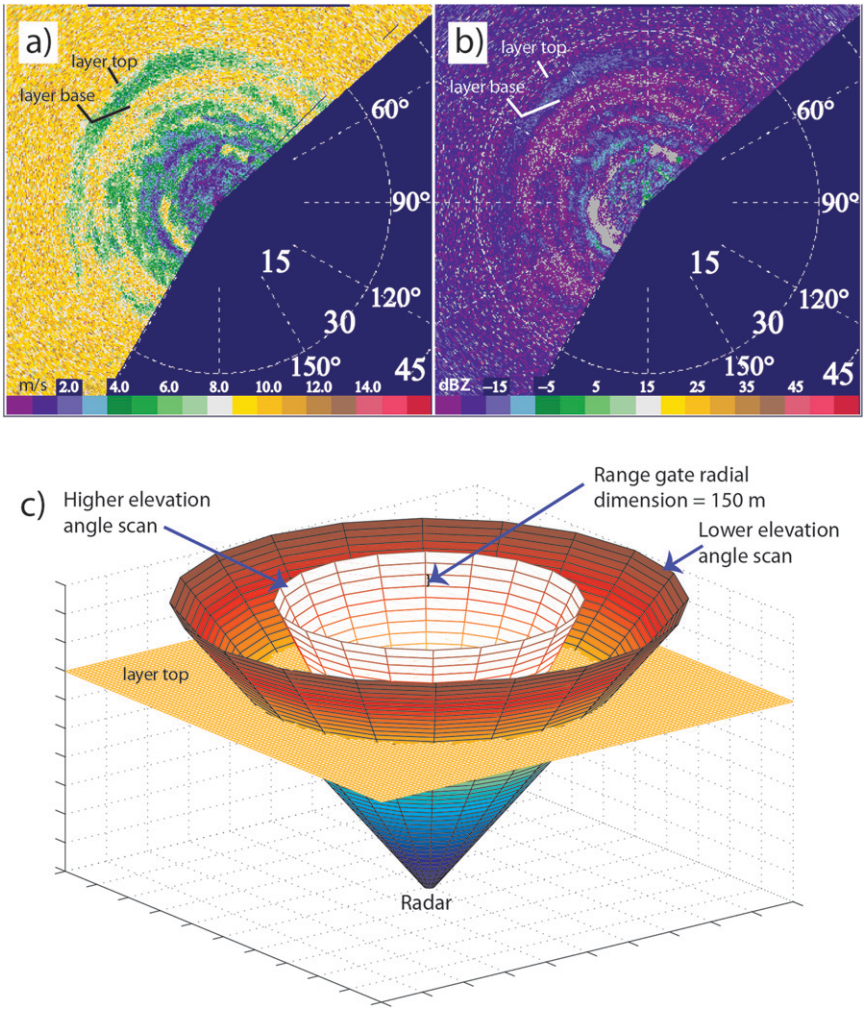

FIG. 1. Sector scan at 7.5° elevation angle showing (a) spectral width ($m\,s^{-1}$) and (b) the equivalent radar reflectivity factor (dBZ) measured by the S-Pol radar at 0005 UTC 23 Jan 2005. The range is given in kilometers. (c) The radar volume geometry illustrates how rings are indicative of layered structure when the radar is operating in PPI mode.

delineate aspects of its mesoscale structure. Because RH has historically been a key variable used to characterize the TMBL (see Part I for key papers summarizing trade wind research), we recast the equation for the vertical gradient of radio refractivity N in terms of RH and examine the sensitivity of the terms for the trade wind environment. We demonstrate that above the mixed layer, the vertical RH gradient term dominates and therefore is a significant contributor to the observed BSLs. Finally, we establish a relationship between BSL boundaries and vertical RH profiles using the derived radar BSL boundary altitudes and the large dataset of surface-based soundings and aircraft-released dropsondes from RICO.

In Davison et al. (2013b, hereafter Part III), we provide statistical analyses of BSL characteristics and examine their behavioral trends as a function of rain rate and other surface meteorological variables. Based on these statistics, the analyses herein, and the results of Part I, we provide a revised conceptual model of the TMBL that incorporates the observed layering.

2. Data sources

Data from the National Center for Atmospheric Research (NCAR) S-band 10-cm-wavelength, dual-polarization Doppler radar (S-Pol), deployed on Barbuda during RICO between 24 November 2004 and 24 January 2005, were used in this study (Fig. 2). Table 1 summarizes the characteristics of the radar during its RICO deployment. The radar used two different scan types: 1) the plan position indicator (PPI) scan, which swept a sector less than 360° (typically about 180°) at elevation angles ranging

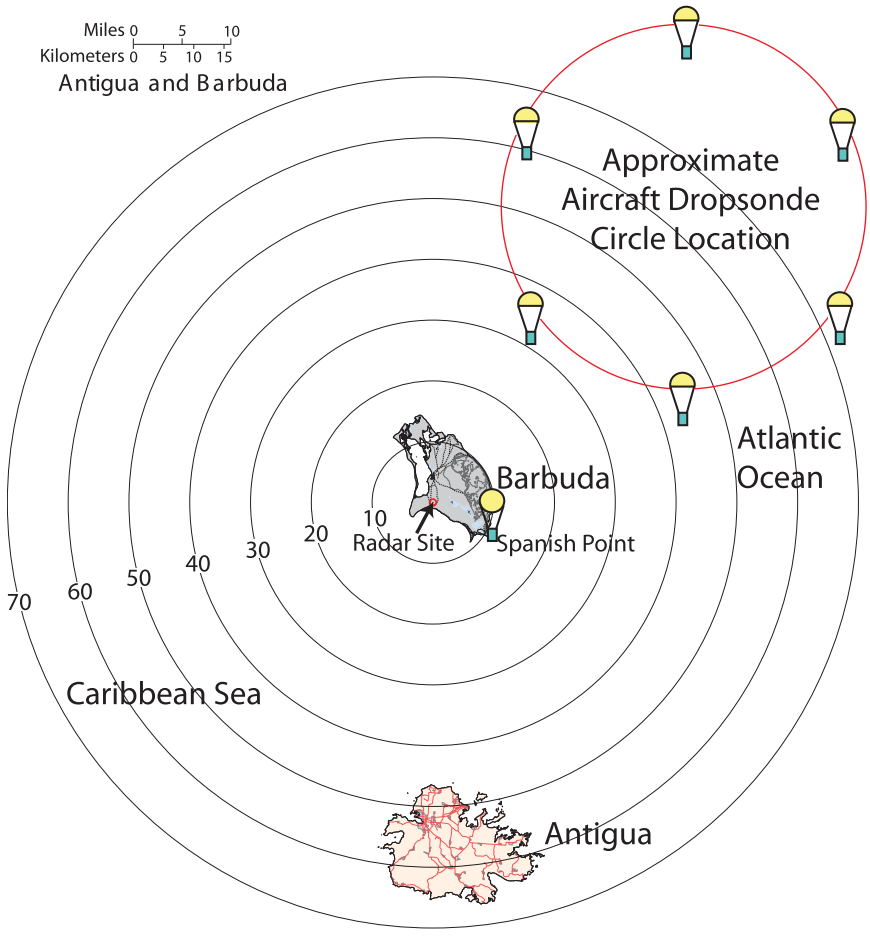

FIG. 2. Map of Antigua and Barbuda showing the locations of 1) the most common rawinsonde launch site, Spanish Point (green rectangle); 2) the radar site (red dot), where S-Pol was deployed and rawinsondes were occasionally launched; and 3) the approximate release pattern and location of the C-130 dropsonde circle. Range rings are in kilometers.

from 0.5° to 16.9° (e.g., Figs. 1a,b), and 2) the surveillance (SUR) scan, which swept a 360° sector at 0.5°.

Vaisala RS92 rawinsondes were launched from Barbuda at either Spanish Point or the S-Pol site (Fig. 2; see Part I for details). Also, 34 sets of NCAR GPS dropsondes were released over the Atlantic from the NCAR C-130 aircraft along 60-km-diameter circles centered about 65 km northeast of the radar site (Fig. 2). Typically, six dropsondes were launched for each set, all within 25 min, from an altitude of approximately 4.6 km in an evenly spaced pattern along the circle. The dropsondes used the Vaisala RS90 pressure–temperature–humidity sensor module [RSS903; see Verver et al. (2006) and Luers (1997) for error characteristics] and the GPS receiver module (GPS111). The final RICO quality-controlled sounding dataset used in this analysis consisted of 131 rawinsondes and 196 dropsondes. Loehrer et al. (1996, 1998) describe quality control procedures used for the RICO dropsonde data.

3. Scattering mechanism associated with layered radar echoes

Radar echoes arise from both Bragg scattering associated with the turbulent mixing of air with different indices of refraction and Rayleigh scattering from hydrometeors, birds, insects, and other particulates including

TABLE 1. S-Pol radar characteristics during RICO.

Deployment dates	24 Nov 2004–24 Jan 2005
Latitude	17.5511°
Longitude	−61.7372°
Altitude	12 m MSL
Maximum range	147 km
Beamwidth	0.92°
Range gate spacing	149.89 m
Minimum detectable Z at 1 km (50 km) at a signal-to-noise ratio (SNR) of −6 dB	−52 (−15) dBZ

haze drops (e.g., Knight and Miller 1993, 1998). Bragg scattering occurs when air parcels with different moisture and/or temperature characteristics are turbulently mixed, producing index of refraction gradients at half the wavelength of the radar (e.g., Doviak and Zrnić 1984). According to theory, fine gradients with dimensions within the inertial subrange arise because the turbulent energy cascade happens much more quickly—by several orders of magnitude—than thermal and moisture diffusion (e.g., Tatarski 1961).

During RICO, radar measurements were made over open ocean from a small island. Insect echoes were virtually nonexistent. This was easily confirmed using differential reflectivity. Bird echoes were present but appeared in single random range gates or along fine lines, and typically exhibited high reflectivity. They were never organized in layers such as those appearing in Figs. 1a and 1b. Layers such as those in Figs. 1a and 1b were common on all days during RICO, independent of cloud cover, so long as the radar domain was not completely cloud filled and swamped with Rayleigh echoes from cloud particles. Therefore the source of the echoes producing the layers is either Bragg scattering or Rayleigh scattering from haze.

To determine the primary scattering mechanism(s) producing the layers, we calculated the Rayleigh radar reflectivity from aerosol particle size distributions as a function of altitude and distance from cloud. The details concerning the measurements of the particle size distributions are given in Rauber et al. (2013). The distributions were determined by averaging aerosol spectra obtained in clear air adjacent to every cloud sampled during 14 RICO C-130 flights. The particle size distributions were calculated from the forward-scattering spectrometer probe (FSSP) and the passive cavity aerosol spectrometer probe (PCASP) data. The FSSP size distributions were measured at ambient RH. The PCASP measures particle sizes at about 40% RH (e.g., Strapp et al. 1992; Snider and Petters 2008). The PCASP particle size distribution of each 10-Hz sample was adjusted using the Köhler equation from an assumed value of RH of 40% at the probe optics to the ambient RH at the time and location where each individual spectrum was measured. The details concerning the calculations using the Köhler equation are given in Rauber et al. (2013). Figure 3 shows the results.

The maximum radar reflectivity values were found to occur near clouds where RH is highest and the haze particles are largest (Rauber et al. 2013). The maximum calculated value of reflectivity contributed by the haze particles was about −55 dBZ. At all other distances from cloud at the altitudes sampled, the values were −55 dBZ or less. This is below the minimum detectable reflectivity

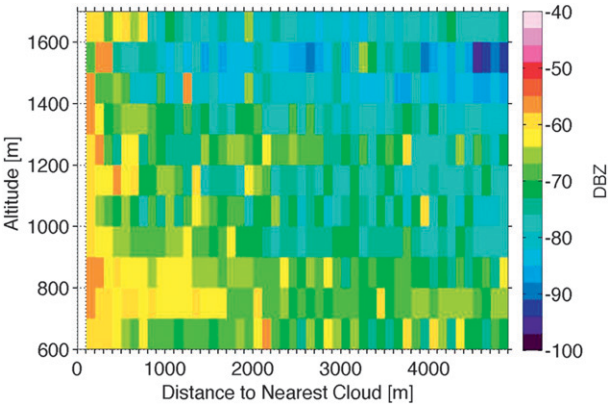

FIG. 3. Radar reflectivity factor derived from particle size distributions measured as a function of altitude and distance from cloud. The particle size distributions were derived from FSSP measurements at ambient RH and PCASP measurements corrected to ambient RH. The data were from all cloud penetrations made during 14 C-130 flights in RICO.

of S-Pol at 1 km (see Table 1). In addition, Snodgrass et al. (2009, their Fig. 11) overlaid data from S-Pol with data from the Multiangle Imaging Spectroradiometer (MISR) aboard the *Terra* satellite platform for all available scenes during RICO, and determined the statistical distribution of radar reflectivity for the clear-air RICO environment using a clear conservative cloud mask that minimizes cloud contamination. Their data showed that the clear-air echo distribution was Gaussian with a mean of −11 dBZ and a minimum in the tail of the distribution at −23 dBZ. The values reported by Snodgrass et al. (2009) are much higher than, and completely distinct from, the values calculated from the particle size distributions. We therefore conclude that Rayleigh scattering from haze particles is not responsible for the layered radar echoes. By process of elimination, we conclude that the clear-air echoes result from Bragg scattering.

There is historical evidence supporting this claim. The use of S-band radar to investigate clear-air structure using Bragg scattering was first explored in the mid-1900s (Ottersten 1969 and references therein). These studies showed that scattering layers were common in clear air using 10-cm or longer wavelength radars. Layers were noted at thicknesses from tens to a few hundred meters, with as many as 10 layers appearing in a single radar scan below 6-km altitude. Ottersten (1969) labeled the layers as ''turbulent structures in the stable regime,'' and linked them to regions of increased static stability. He noted that when significant water vapor gradients were present, only a minimal amount of turbulence was necessary to produce radar echoes. Many of these early measurements were made at either Wallops Island, Virginia, or Aberystwyth, Wales, and thus were characteristic of marine environments.

A series of papers by Gossard et al. (1982, 1984a,b, 1985) examined turbulent structures detected by S-band radar in thermally stable regions. Gossard et al. (1984b, 1985) examined tower data from Boulder Atmospheric Observatory in conjunction with frequency modulated–continuous wave (FM-CW; 10 cm) radar and acoustic sounder data. Their findings clearly showed BSLs coinciding with temperature inversions. The inversions in their study showed a high negative correlation to water vapor mixing ratio. In a review article, Chadwick and Gossard (1986) noted that 10-cm and longer wavelength radars have the capability of identifying the mixed-layer top in a turbulent boundary layer. Heinselman et al. (2009) exploited this idea to identify the elevation of the mixed-layer top in Oklahoma.

4. Detection of BSLs

Rayleigh scattering in the atmosphere ranges from the lowest detectable signal to around 70 dBZ, and Bragg scattering extends from the lowest detectable signal to around 10 dBZ at S band, as so far documented (e.g., Knight & Miller 1993, 1998; Snodgrass et al. 2009). Because Bragg scattering returns were the phenomena of interest, range gates with equivalent reflectivity greater than 10 dBZ were excluded to eliminate precipitation contamination (Knight and Miller 1993). The value 10 dBZ was used rather than a lower cutoff because, during RICO, trade wind cumuli radar echoes were often observed to preferentially detrain into and enhance preexisting BSLs and were most likely due to both Bragg and Rayleigh scattering. The relationship between cloud detrainment and BSLs is discussed in more detail in section 6. The vast majority of clouds in the RICO trade wind environment were confined beneath the top of the transition layer, nominally within the lowest kilometer above sea level (Zhao and Di Girolamo 2007), and thus had no direct influence on BSLs above the transition layer. However, as we will show in Part III, shallow clouds within the transition layer most likely lead to a mix of Bragg and Rayleigh scattering in this layer. Above the transition layer, most equivalent radar reflectivity values less than 10 dBZ generally coincided with the BSLs.

To estimate the altitudes of BSL bases and tops, an algorithm based on the Haar wavelet was employed (e.g., Kumar and Foufoula-Georgiou 1997). The Haar wavelet is especially advantageous for analyzing signal transitions, such as the boundaries of BSLs observed in the RICO data. The Haar wavelet analysis was carried out on each beam of data in every PPI scan at elevation angles 5° and greater for the entire RICO project. Details of the analysis procedure are provided in the appendix. During RICO, the BSLs appeared in both the equivalent radar reflectivity and spectral width fields but were more sharply defined by spectral width (Figs. 1a,b). Spectral width values within the BSLs were typically less than 6 m s^{-1}, while layers with no coherent power return to the radar had spectral width values of about 10 m s^{-1}. Thus, spectral width was chosen as the variable on which the calculations were performed.

5. Temporal layer structure

A spatially and temporally independent estimate of each BSL upper and lower boundary was generated for each elevation angle scanned. Once the BSL bases and tops were found, their elevations were plotted as a function of time (see Figs. 4–6). The results from all elevation angles 5° and greater were superimposed on the figures to provide multiple independent estimates of the temporal structure of the BSLs. The general close agreement between edge elevations found from scans with different elevation angles indicates that relatively distinct boundaries between atmospheric layers were present within the radar domain. One significant revelation from such plots is the long-lived nature of the BSLs in the RICO environment.

The number of wavelet iterations determines the degree of smoothing and, thus, the degree to which weak transitions will be retained in the analysis (cf. Figs. 4a and 4b). The time–height plot shown in Fig. 4c has combined results from four (Fig. 4a) and five (Fig. 4b) wavelet iterations. Experiments showed that four iterations could detect many thinner BSLs not seen in the results using five iterations, although the five-iteration results were significantly less noisy. For this reason, we chose to use both the four- and five-iteration estimates to achieve the best possible depiction of where the BSLs were located.

Many diagnostic characteristics of the TMBL can be observed using such plots. In Fig. 4c, as many as five BSLs can be observed above the transition layer at a given time, and the lifetime of most exceeds 10 h. The top of the transition layer (denoted by red dots capping the blue shaded region) is seen to increase in altitude throughout the 24-h period. The BSL labeled A at the onset is seen to subside and/or slope downward beginning just prior to 0400 UTC. Around 0500 UTC, it is replaced as the top layer when two new BSLs, B and C, either developed within or moved into the radar domain. BSL D, sandwiched between A and E, appears to become compressed, to the point where it is no longer detectable at 0800 UTC. BSL E begins to thin shortly afterward. BSL D becomes detectable again at 0900 UTC and appears to expand, perhaps caused by an influx of moisture into it from cloud detrainment somewhere upwind. The two BSLs, A and D, appear to merge just

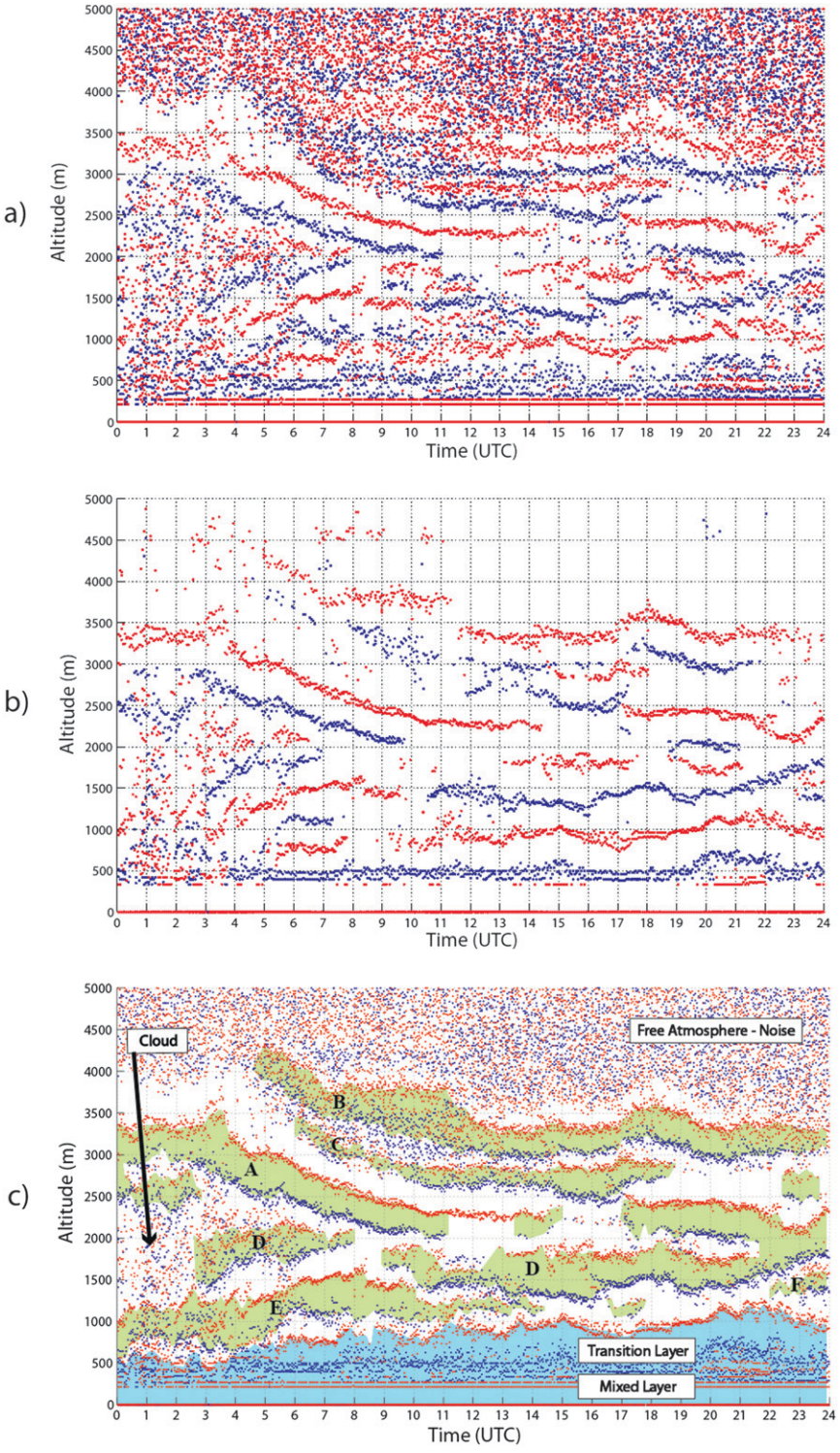

FIG. 4. Time–height diagram of BSL edge locations from 23 Dec 2004. (a) The results from the fourth wavelet iteration, (b) the results from the fifth wavelet iteration, and (c) the combined results of both fourth and fifth wavelet iterations. Coherent lines of red (blue) dots indicate the upper (lower) edges of BSLs. In (c) green shading indicates BSLs, white shading indicates regions where radar echoes are below the noise threshold, and the light blue shading denotes the mixed layer (below blue dots) and transition layer (above blue dots). Noise appears as random red and blue speckles. Local time is UTC − 4 h. Sunrise and sunset occur near 1000 and 2200 UTC, respectively.

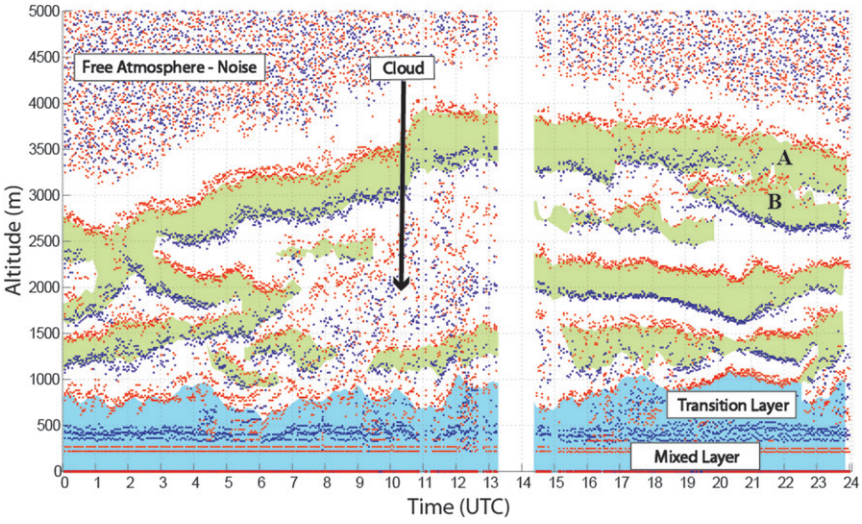

FIG. 5. Time–height diagram of BSL edge locations from 1 Jan 2005. The shading is as in Fig. 4c.

after 2100 UTC. At 2200 UTC, a new BSL, F, either develops or moves into the radar domain just below the merged one and appears to displace the merged BSL upward as it emerges.

As with any averaging procedure, inhomogeneities in the environment can lead to obscure results that require examination of the original or supplementary data for correct interpretation. For example, in Fig. 5 after 1900 UTC and near 3000 m, two BSLs, labeled A and B, appear to overlap. Looking back at the original radar scans, we can see that this is due to asymmetry in the ring patterns of the two outermost BSLs (Fig. 7). Conversely, the partial ring seen nearer the center of the radar cone in Fig. 7 is clearly detected in Fig. 5 just below 1500 m. Unlike Fig. 4, the day portrayed in Fig. 5 is more characterized by the ascent of the uppermost BSL rather than descent. The uppermost BSL has its minimum altitude near 2600 m around 0100 UTC and grows to roughly 4000 m near sunrise (1000 UTC). This day is distinguished by many rapid transitions in altitude of thin, sharply defined BSLs. Interspersed are times when significant cloud cover was present, and the BSL structure could not be determined.

In contrast to Figs. 4 and 5, Fig. 6 shows a day with many BSLs, extending up to 4.5 km. Both the uppermost BSL and the individual BSLs below it maintain their altitudes and do not vary much over the course of this day. Additionally, the BSL edges on parts of this day

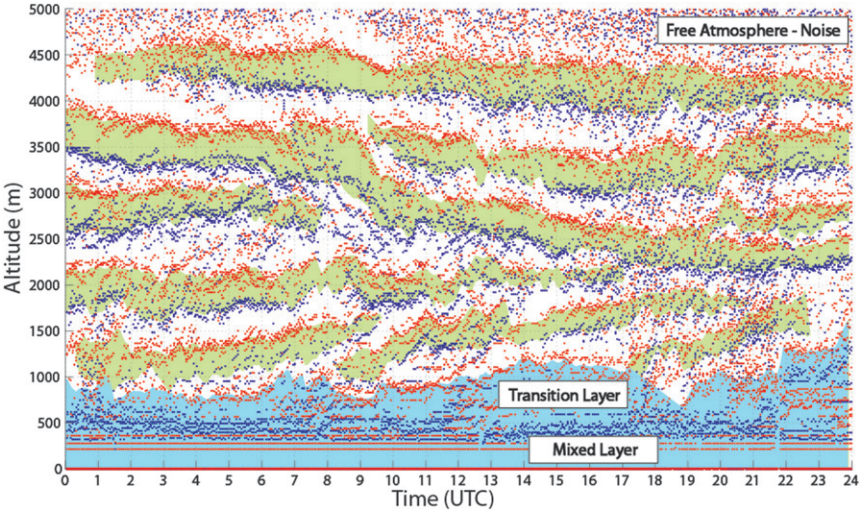

FIG. 6. Time–height diagram of BSL edge location from 17 Jan 2005. The shading is as in Fig. 4c.

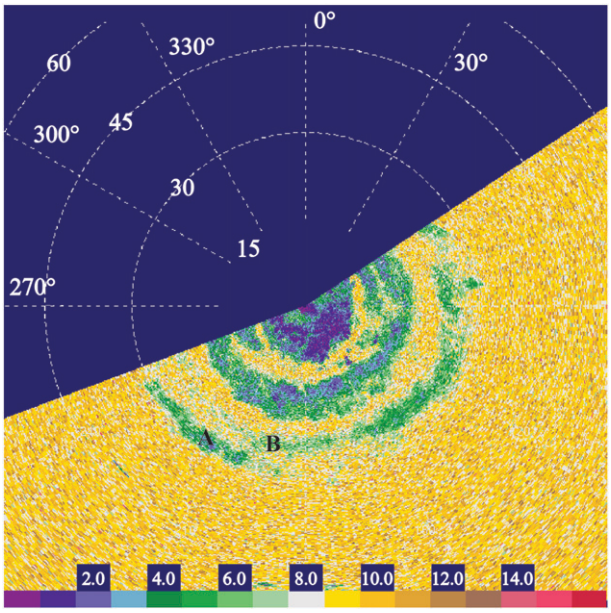

FIG. 7. PPI scan of spectral width ($m\,s^{-1}$) for the 6.8° elevation angle at 2102 UTC 1 Jan 2005. The range is given in kilometers. The two outermost rings are asymmetric and give rise to the overlapping layers in Fig. 5. A partial ring is also apparent just inside the 15-km range ring.

appeared less crisp. There were two causes. The first is that the sector scans changed either in location or in number of total angles scanned. Such transitions can be seen on Fig. 6, for example, just before 2200 UTC. The second is due to clouds that were not completely filtered. Examination of individual PPIs show that when clouds are present but do not have sufficient coverage to disrupt the BSLs, the range of BSL edge estimates widen, generating a more ragged appearance.

6. Relationship of the BSLs to vertical gradients of RH

a. *Turbulence and the development of vertical RH gradients*

We can understand how large negative vertical gradients of N and RH come about by considering the effects of turbulent mixing on a layer with initially constant lapse rates of specific humidity q and potential temperature θ. Consider a vertical atmospheric profile within the TMBL characterized by constant lapse rates of both potential temperature, $d\theta/dz = C_1$, and specific humidity, $dq/dz = C_2$ (see Figs. 8a,c). If a layer of continually forced turbulent mixing is imposed within this profile with no influx of heat or moisture, then within the core of the turbulent layer, the gradients $d\theta/dz$ and $dq/dz \rightarrow 0$ (see Figs. 8b,d). Near the upper and lower boundaries of the turbulently mixed region, strong vertical gradients of both θ and q would develop. As a consequence, two regions of increased static stability (and possibly temperature inversions) would form (between θ_1 and θ_2 and between θ_3 and θ_4 in Fig. 8b). These regions of increased static stability would also be characterized by more negative dq/dz, radio refractivity dN/dz, and especially $d(\mathrm{RH})/dz$ than the initial gradients since the temperature at the top (θ_3 elevation) and bottom (θ_2 elevation) of the turbulent layer core would be colder and warmer, respectively, after mixing. We can therefore infer that in many cases a layer of increased turbulence (e.g., due to vertical shear) can modify the RH profile such that the two layers of increased static stability bounding the turbulent layer will each be characterized by an RH maximum near its base and an RH minimum near its top. Based on analyses presented below in section 6c, these layers of increased static stability would favor the production of BSLs.

In contrast, within the core of the turbulently mixed layer, as $d\theta/dz$ and $dq/dz \rightarrow 0$, the tendency toward homogenization of θ and q will lead to an increase in RH with altitude and a positive tendency in dN/dz. These tendencies would lead to a reduction in the potential for Bragg scattering with time in the core of the turbulent layer. Thus, the turbulent-layer core, which is characterized by an RH minimum at the base and maximum at the top, would be less likely to produce a BSL. The BSLs forming through the turbulence mechanism described above will be layers of enhanced static stability. Indeed, BSLs have been linked to statically stable layers in past studies (e.g., Ottersten 1969).

b. *Cloud detrainment and the development of vertical RH gradients*

Temperature inversions and other layers of increased static stability are known to inhibit cloud development and cause detrainment of cloudy air and water vapor near the bases of the layers (e.g., Perry and Hobbs 1996). When trade wind clouds are present, water vapor should be preferentially detrained near the bases of stable layers, thereby helping to create or sustain the BSL structure (Fig. 9). With one cloud, this would be a transient effect, but with fields of clouds such as those common in the trades, the water vapor input might be sufficient to explain the steady state nature of the BSLs.

The radar image in Fig. 10 shows an example of how cloud detrainment might enhance a BSL through injection of water vapor into a layer. The cloud in Fig. 10 appears as a region of enhanced reflectivity with a 20-dBZ core near 50° and 22-km range. There may be a cloudy ''anvil'' region around the cumulus core. Note the two BSLs that intersect the points at 315° and 18- and 28-km

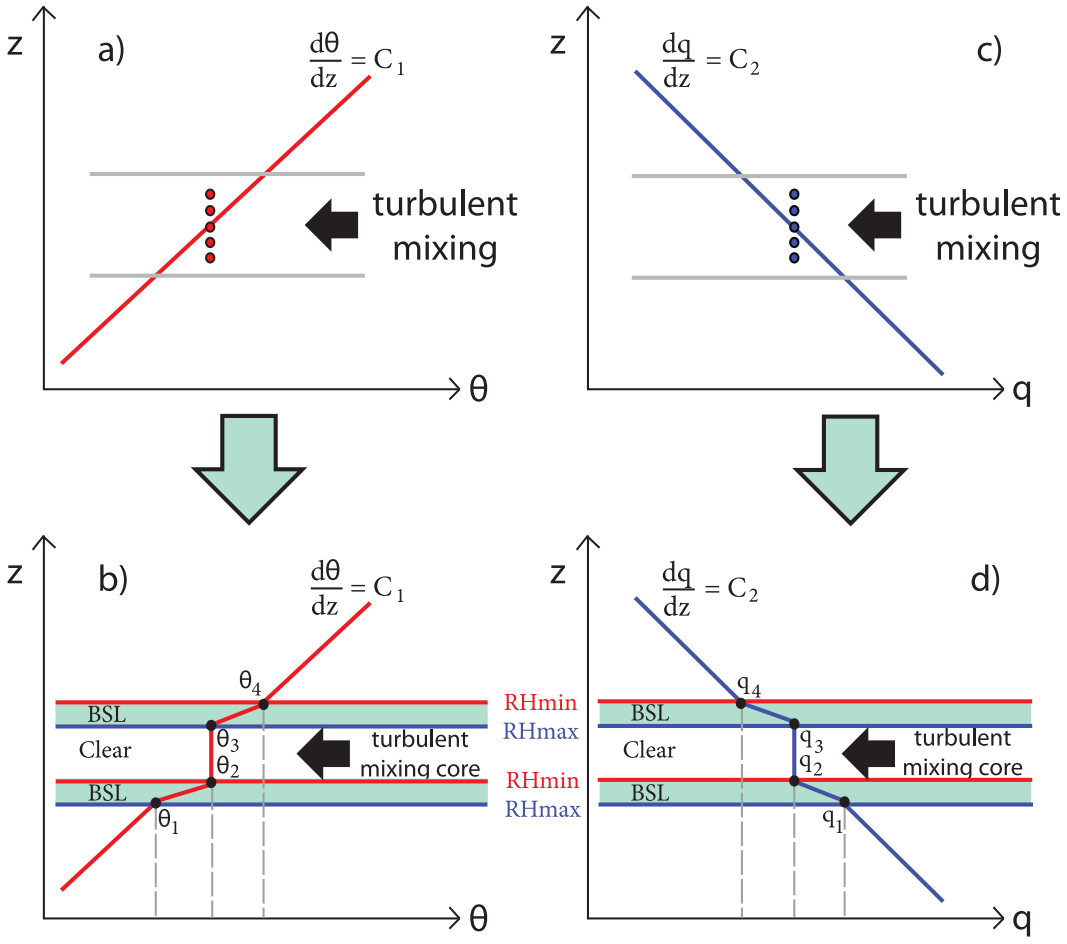

FIG. 8. Cartoon detailing how a turbulent mixed layer imposed on an environment with constant lapse rates of (a) θ and (c) q can generate a layered RH profile and subsequent BSLs with no influx of (b) heat or (d) moisture.

ranges. These two points are 30 and 38 km away from the cloud, respectively, and are unlikely to be part of the anvil cloud at these distances. Detrained water vapor from this cloud and other clouds that may have been present upstream and at earlier times may have contributed to the maintenance of these layers. In Part III, we will investigate the potential role of clouds in maintaining BSLs further using satellite data.

c. *Relationship between vertical gradients of radio refractivity and RH*

Radio refractivity is normally expressed as a function of temperature T, pressure p, and vapor pressure e and is related to the index of refraction n by

$$N = (n-1)\times 10^6 = 77.6\frac{p}{T} - 5.6\frac{e}{T} + 3.75\times 10^5\frac{e}{T^2}, \tag{1}$$

where p and e are in millibars and T is in kelvins (e.g., Bean & Dutton 1968). To interpret the BSLs in terms of the meteorology of the trade wind layer in Part III, we investigate here the relationship between Bragg scattering, BSL structure, and RH.

Contours of constant N as a function of T and e are shown at various pressure levels in Fig. 11. Overlaid are curves of constant RH. These plots demonstrate the good agreement of N and RH slopes at low T and e. At higher T and e, there is poorer slope agreement, but N and RH slopes remain positive. All Barbuda-launched rawinsonde values at the given pressure levels are provided for reference. Note that N is a stronger function of e than T (Fig. 11 and Knight and Miller 1993). Based on the arguments presented in sections 6a,b, we test below whether large vertical gradients of N will generally correspond to large vertical gradients of RH. We investigate this by first deriving a relationship for dN/dz in terms of RH and then performing a scale analysis of the resulting equation to determine the relative importance of the vertical RH gradient term to vertical gradients of N.

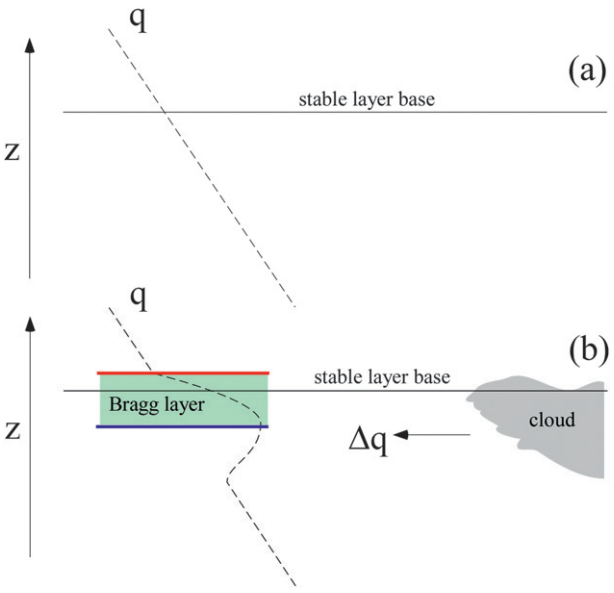

FIG. 9. Cartoon illustrating how detrainment of moisture from trade wind clouds might alter the (a) background distribution to create (b) stronger water vapor gradients near the base of a stable layer.

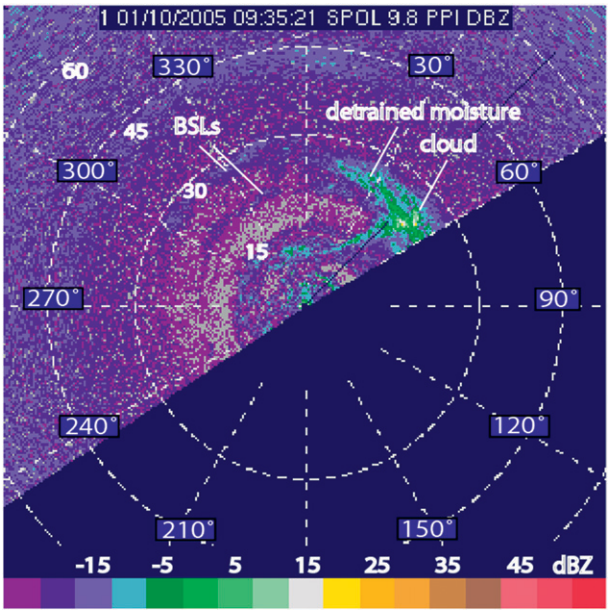

FIG. 10. Radar reflectivity scan (dBZ) showing a cloud, a region of detrainment near the cloud, and BSLs near the detrainment altitude. The BSLs in this case were present prior to the appearance of the cloud based on examination of earlier radar scans.

Multiplying and dividing the last two terms of (1) by the saturation vapor pressure e_s, we obtain

$$N = 77.6\frac{p}{T} - 5.6S\frac{e_s}{T} + 3.75\times10^5 S\frac{e_s}{T^2}, \qquad (2)$$

where S is the saturation ratio (S = RH/100) and e_s is only a function of T. Taking the vertical derivative of (2) and rearranging terms yields

$$\frac{dN}{dz} = \underbrace{77.6\frac{1}{T}\frac{\partial p}{\partial z}}_{\text{A}} - \underbrace{\left(77.6p - 5.6Se_s + 7.5\times10^5\frac{Se_s}{T}\right)\frac{1}{T^2}\frac{\partial T}{\partial z} + \left(-5.6 + 3.75\times10^5\frac{1}{T}\right)\frac{S}{T}\frac{\partial e_s}{\partial z}}_{\text{B}}$$
$$+ \underbrace{\left(-5.6 + 3.75\times10^5\frac{1}{T}\right)\frac{e_s}{T}\frac{\partial S}{\partial z}}_{\text{C}} \qquad (3)$$

In (3), term A is the pressure contribution to dN/dz, term B is the contribution due to vertical temperature gradients, and term C is the contribution due to vertical gradients of RH. Figure 12 shows a frequency by altitude diagram (FAD; see Part I) for $\Delta N/\Delta z$, where Δz = 50 m. Both positive and negative N gradients greater than 10 $(50\,\text{m})^{-1}$ exist in the TMBL, but negative gradients are more common and generally larger in magnitude than positive gradients. This is expected since the near-surface air is adjacent to the ocean, while the higher atmosphere is quite dry, so that the average vertical gradient of e is negative through the whole atmosphere.

The terms A, B, and C in (3), along with $\Delta N/\Delta z$, are plotted at 1000-, 2000-, 3000-, and 4000-m altitudes in Figs. 13 and 14 for soundings in the smallest and largest quartiles in Fig. 12, respectively. The smallest and largest quartiles of $\Delta N/\Delta z$ values are used because these represent the more extreme vertical gradients of N and thus are more likely to coincide with BSLs. In Fig. 13, the pressure term, A, is largely invariant, small, and negative at each altitude. The temperature term, B, exhibits more variability but is generally smaller in magnitude than the pressure term. The RH term, C, is negative, its magnitude is relatively large, and it closely aligns with $\Delta N/\Delta z$.

In Fig. 14, term A again is largely invariant, small, and negative. Term B is again smaller than A, but with more variability. The RH term, C, is nearly always positive

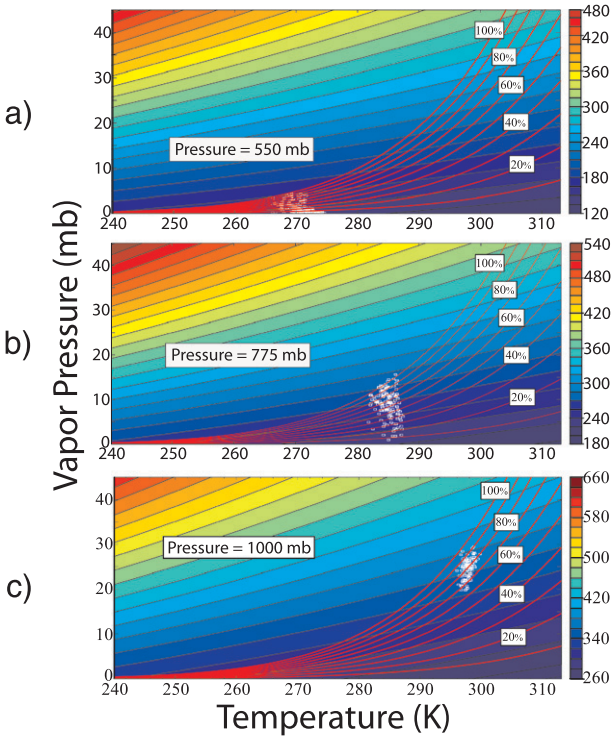

FIG. 11. Color contours of constant radio refractivity for fixed pressure levels of (a) 550, (b) 775, and (c) 1000 mb. Overlaid in red are lines of constant RH. RICO rawinsonde vapor pressure and temperature measurements for the given pressure altitudes are shown for reference (white squares).

and is generally the largest term. In those soundings where $\Delta N/\Delta z$ is positive and relatively large, $\Delta N/\Delta z$ is closely aligned with the RH term, C. However, fewer cases of large positive N gradients exist, since the pressure term always imposes a negative component to the vertical N gradient. For this reason, the values from the largest quartile of $\Delta N/\Delta z$ are generally smaller in magnitude than those in Fig. 13.

Summarizing Figs. 11–14, there are two key points that can be drawn: the large vertical gradients of N required for Bragg scattering 1) will closely coincide with large vertical gradients of RH of the same sign and 2) will more often be negative because the pressure term reinforces the RH term.

7. Relationship between BSL boundaries and RH extrema

Based on the arguments and analyses presented in section 6, we expect that a BSL will exist in the turbulent interface layer between air with lower RH overlying air with higher RH, and furthermore that the base and top of the BSL will be located close to an RH maximum and an RH minimum, respectively. Additionally, we expect that layers that do not satisfy these conditions will be less likely to support detectable Bragg scattering, particularly over long periods. This section is devoted to testing this idea.

In this section, sounding RH profiles will be compared to the radar layers to quantitatively assess the relationship between the RH profile and Bragg layers. Two questions need to be answered to reasonably attempt the comparison: 1) what constitutes significant RH extrema in the soundings that might provide the bounds for a BSL detectable by the radar, and 2) how well do RH measurements from a single sounding represent the moisture field in the ambient environment near the radar?

a. Determining RH extrema in soundings

To compare RH profiles from soundings with radar-observed BSLs, we first need to define the vertical boundaries of proxy BSLs in soundings based on extrema in their RH profiles. To determine extrema, RH profiles from all soundings were first linearly interpolated from their original approximately 5–7-m vertical resolution to 1-m resolution. The same wavelet technique applied to individual radar beams was then applied to each sounding for seven iterations, yielding a Haar mother wavelet W_m for each sounding. Seven levels of iteration effectively filtered variations in the RH field at scales below 64 m. This value is slightly larger than the vertical projection of a radar pulse volume (43 m) when the beam elevation angle is 16.9°—the maximum used in RICO. Figure 15 shows an example of an interpolated sounding, the corresponding filtered sounding, and cW_m, where $c = (\sqrt{2}/2)^7$—a constant determined by the wavelet technique. Extrema in RH were selected based on an analysis of the cW_m curve. Extrema occur where the cW_m curve crosses zero, with RH maxima occurring below regions with positive area (e.g., blue lines on Fig. 15) and RH minima occurring above regions with positive area (e.g., red lines on Fig. 15). The vertical extent and magnitude of the positive area is related to the vertical gradient of RH across a layer. The vertical gradient of RH, in turn, is indicative of index of refraction gradients capable of producing Bragg scatter. As seen in Fig. 15, both small and large fluctuations in RH occur in the vertical. We are interested in those fluctuations that occur on scales comparable to the depth of the Bragg layers detected by the radar. To eliminate small-scale fluctuations in the following analysis, tests were performed using the value of the positive area (region between the positive portion of the cW_m curve and the $cW_m = 0$ line) as a threshold to define a proxy BSL. Based on these tests, a threshold area of 175 %RH m was chosen as the minimum area required to define a single proxy BSL. This method retained extrema associated with large moisture

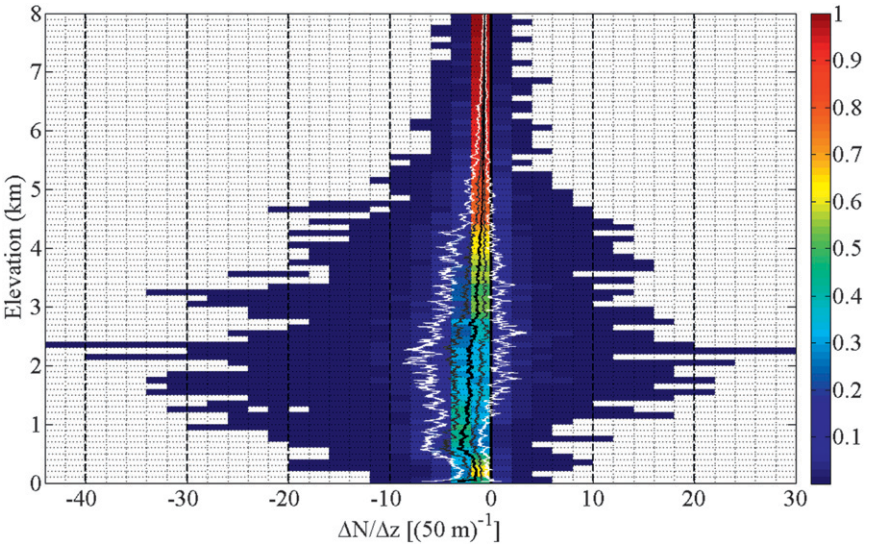

FIG. 12. FAD of $\Delta N/\Delta z$ for $\Delta z = 50$ m for all the Barbuda-launched soundings during RICO. Overlaid are the median (black), 25th and 75th percentiles (dark gray), and 10th and 90th percentiles (white).

gradients across shallow vertical layers and smaller moisture gradients over deeper layers, while effectively removing small-scale variations over shallow layers. If the minimum vertical separation between two consecutive proxy BSLs was less than 150 m, they were combined into a single layer if the absolute value of the negative area between them was less than 50% RH m. The reasoning for this choice was that unless the layers were extremely distinct (as implied by large negative area between them), they would most likely be irresolvable by the radar at this fine a vertical separation. Layers not satisfying all the above criteria were assumed to be clear (i.e., layers without coherent radar echo).

b. *Moisture variability on the scale of the radar domain*

The examples of evolving BSLs presented in section 5 suggest that BSLs in general are not necessarily homogeneous in space and time. Layers can ascend or descend with time, move into or out of the radar domain, combine with other layers, and form or dissipate. Within a single radar scan or volume, layers might be tilted, vary in thickness, or fill only part of the domain. A sounding provides a single profile through the radar domain that may or may not be representative of the moisture field within the radar volume containing the BSLs. To test the relationship between BSL edges and RH extrema using soundings, we must first determine the probability that a BSL identified by the radar will coincide vertically with a proxy BSL identified from analysis of a single sounding. Even if the relationship between BSL edges and RH extrema exists, the soundings and radar might not agree depending on the amount of variability in the RH field over the scale of the radar domain.

The RICO dropsonde dataset provided a unique opportunity to investigate the representativeness of individual soundings by quantifying the variability of the moisture field in an environment on the scale of the radar analysis domain. To quantify this variability, we conducted statistical comparisons of the near-coincident dropsondes launched around the 60-km-diameter circles (Fig. 2). Specifically, we determined the probability that a proxy BSL identified in the mean profile of a dropsonde circle set will coincide vertically with a proxy BSL identified from analysis of a single dropsonde within the set. The statistics derived from this analysis provide a quantitative guide as to what should be considered reasonable agreement between the radar and single-sounding-derived BSLs.

To analyze the dropsondes, RH extrema were found for each dropsonde using the method presented above in section 7a. The extrema determined from each dropsonde were compared to extrema determined from an analysis of $W_m^* = \sum_{n=1}^{x} W_m(n)$, where x is the number of dropsondes in a particular set launched around a single circle (see appendix for mathematical definition of W_m). The sum was used rather than the average to reduce the likelihood that nonhomogeneous layers would be eliminated through vertical phase cancelation when the 175% RH m area threshold was applied. The 60-km-diameter circle encompassed by each dropsonde set is close to the average horizontal region encompassed by the radar analysis. The large, positive regions of W_m^*, which represent mean conditions over the area of the

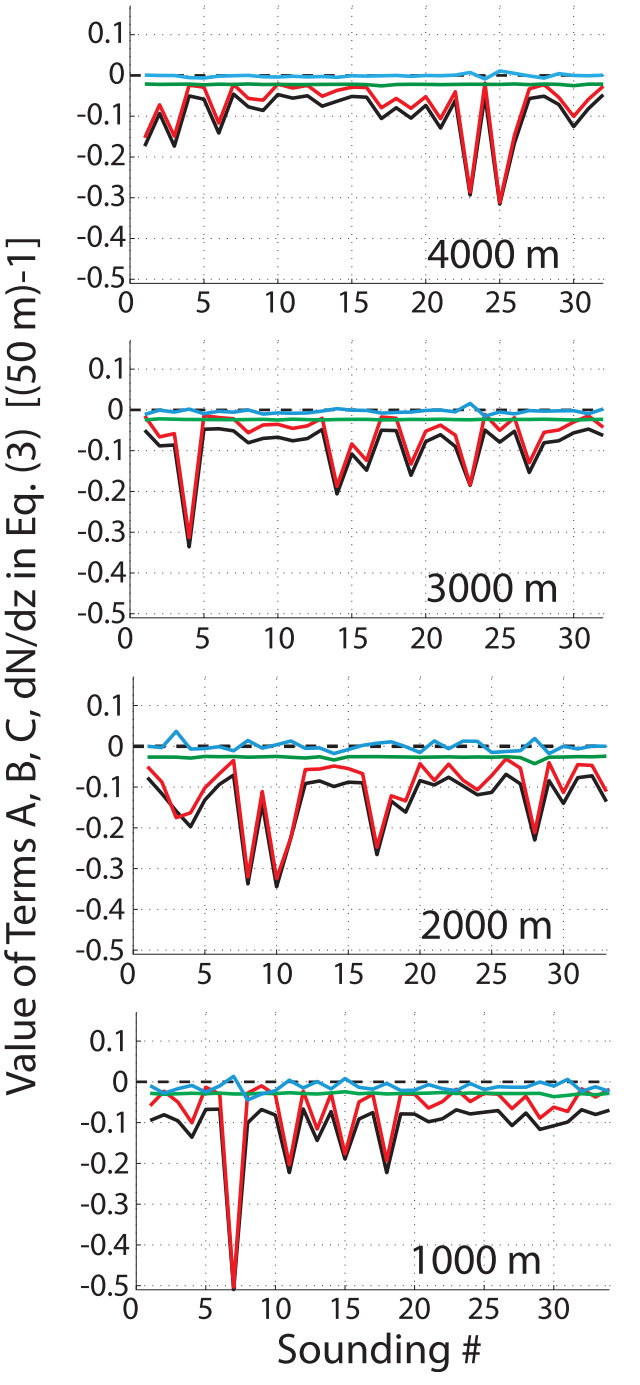

FIG. 13. Contributions of the vertical pressure (term A, green), temperature (term B, blue), and RH (term C, red) gradient terms to $\Delta N/\Delta z$ (black) in (3), plotted at 1000-, 2000-, 3000-, and 4000-m altitude for soundings in the smallest quartile in Fig. 9.

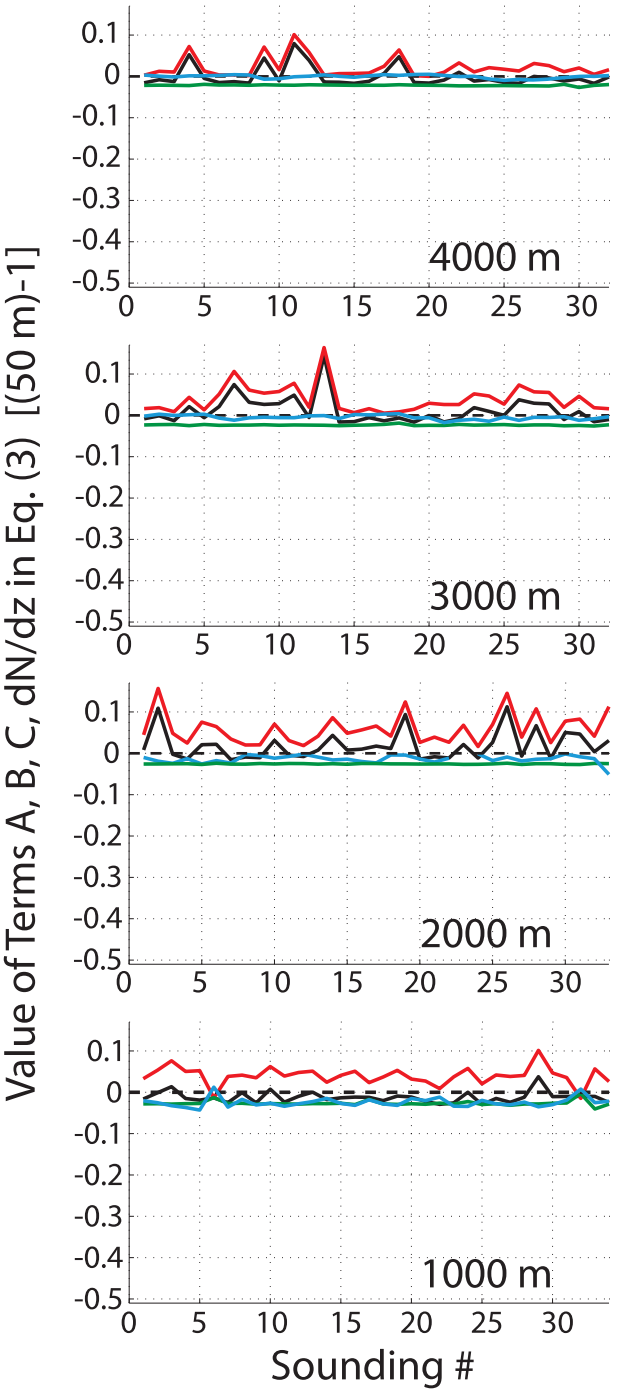

FIG. 14. Contributions of the vertical pressure (term A, green), temperature (term B, blue), and RH (term C, red) gradient terms to $\Delta N/\Delta z$ (black) in (3), plotted at 1000-, 2000-, 3000-, and 4000-m altitude for soundings in the largest quartile in Fig. 9.

circle, each serve as a mean proxy BSL for the BSLs observed by radar.

Our first step in quantifying the variability was to compare the mean proxy BSLs to proxy BSLs determined from single dropsondes in the set. If one W_m^* profile contained 6 proxy BSLs and there were 6 dropsondes in that particular set, then the set contained a total of 36 possible layer matches. For a mean proxy BSL to be matched with a

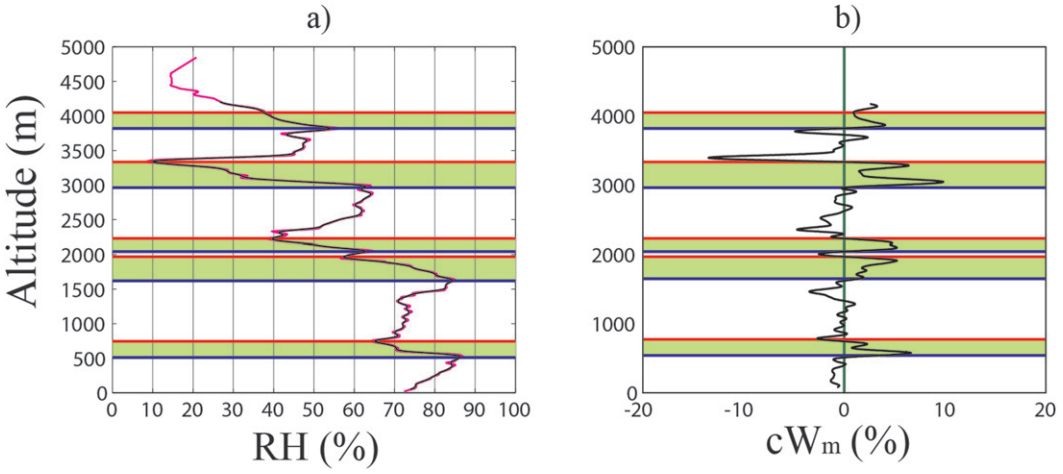

FIG. 15. (a) Interpolated RH profile (magenta) and wavelet-smoothed RH profile (black) for RICO research flight 06, circle 1, dropsonde 5 (1452:57 UTC 16 Dec 2004). The magenta and black lines nearly overlap. (b) cW_m profile (black) for dropsonde shown in (a). Green shading indicates proxy BSLs, bounded below by local RH maxima (blue lines) and above by local RH minima (red lines). The locations of these BSLs are determined by the zero crossings of the cW_m curve bounding positive regions with areas of at least 175% RH m. In this instance, the topmost layer would not have been included in the statistics since the topmost BSL has no zero crossing in the cW_m curve.

proxy BSL from a single dropsonde, we made the requirement that at least 50% of the depth of one BSL be coincident in altitude with that of the other (e.g., Figs. 16a–e). Otherwise, the layers were classified as unmatched (e.g., Figs. 16f–j). Table 2 summarizes the results. For the 34 sets of dropsondes, there were a total of 1157 possible layer matches. Of these, 770 or 66.6% matched. The remaining 387 or 33.4% were unmatched, despite the close proximity in space and time of the dropsonde launches. This high level of variability is evident in the RH profiles shown for four sets of dropsondes in Fig. 17. The largest RH differences in each set for measurements at the same altitude correspond to differences in mixing ratio ranging from 7 to 8 g kg^{-1}. Although Fig. 17 shows some of the more extreme examples, these profiles illustrate well the variability found in the dropsonde sets collected during RICO.

An additional method to characterize the variability was to compare the altitudes of RH maxima and minima bounding the mean proxy BSLs with those from individual dropsondes. This is different from the layer comparison above because, even with a matched layer, it is possible that an RH minimum bounding a mean proxy BSL may be closer in altitude to an RH maximum from an individual dropsonde, or vice versa (Fig. 16). In Fig. 16b, the RH minimum at the top of a mean proxy BSL is closest in altitude to an RH maximum in a single sounding. In Fig. 16c, the reverse is true; the RH maximum at the base of the mean proxy BSL is closest to an RH minimum in the sounding. In Fig. 16d, both the maximum and the minimum in the mean proxy BSL are closest to their opposite extrema. In all three cases, the mean proxy BSL and a sounding proxy BSL met the criteria for a layer match. Analogous situations can occur for unmatched but overlapping layers (Figs. 16g–i). There were 1157 RH maxima and 1112 RH minima matches possible for the proxy BSLs. The difference was due to insufficient data available to determine the altitudes of the topmost RH minima in a few soundings (e.g., Fig. 15).[1]

When single or multiple proxy BSLs from a single sounding were entirely within one mean proxy BSL, or vice versa (Fig. 16e), both tops and bases were considered matched. A maximum (minimum) in RH bounding a proxy BSL was also considered matched if the nearest extremum in altitude on a particular dropsonde was also a maximum (minimum) and the mean proxy BSL overlapped the dropsonde's proxy BSL (Fig. 16). If the BSLs overlapped, but the nearest extremum on the dropsonde vertical profile was opposite, it was classified as mismatched. If the mean proxy BSL was not overlapped by any proxy BSL in a particular dropsonde, both extrema from the mean proxy BSL were classified as unmatched (Fig. 16j). Table 2 summarizes the statistics for the extrema. Approximately 60% of both extrema matched, 28% were unmatched, and 11% were mismatched, again despite the close proximity in space and time of the dropsonde launches. This again illustrates the variability of RH commonly found in the TMBL within a 60-km-diameter

[1] This generally occurred when the TMBL top exceeded 4174 m—an altitude determined by the wavelet technique and the limited peak altitude of the dropsondes.

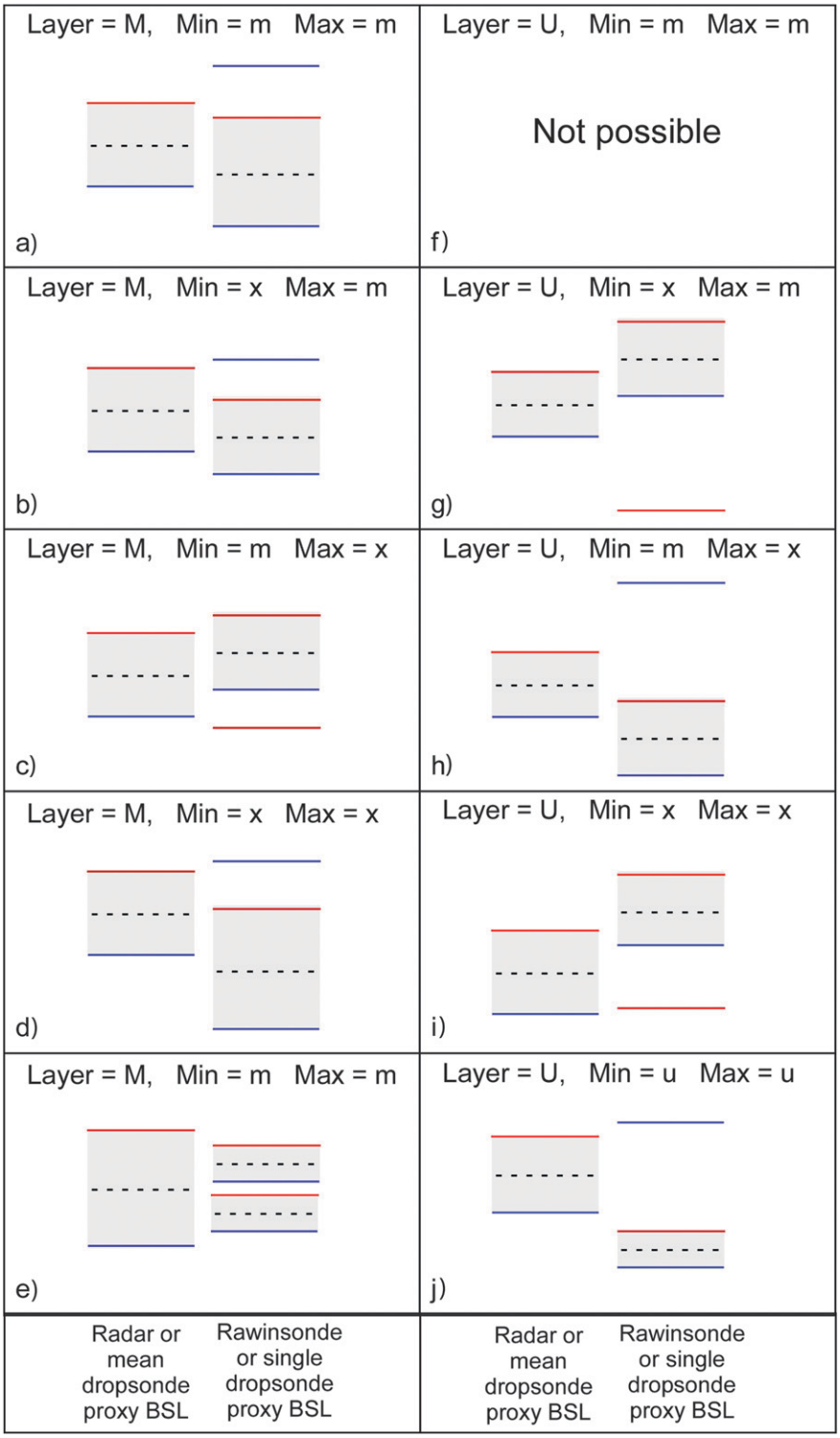

FIG. 16. Examples of how BSLs (mean dropsonde or mean radar) compare in altitude with proxy BSLs (single dropsonde or single rawinsonde). In each panel the left BSL represents the mean and the right represents the individual sounding. (a)–(e) BSLs that match (layer = M) and (f)–(j) BSLs that are unmatched (layer = U). Red (blue) lines denote BSL tops (bases). BSLs are shaded gray and their midpoints are demarcated by dashed lines. For BSL edge comparisons, min = (m, x, u) denotes that the mean layer top is (matched, mismatched, unmatched). Max = (m, x, u) denotes that the mean layer base is (matched, mismatched, unmatched).

TABLE 2. Proxy BSL–dropsonde comparison.

Layer comparison	
Total layers	1157
Matched layers (M)	770 (66.6%)
Unmatched layers (U)	387 (33.4%)

Extrema comparison	RH max	RH min
Total possible matches	1157	1112
Matched (m)	713 (61.6%)	662 (59.5%)
Unmatched (u)	322 (27.8%)	320 (28.8%)
Mismatched (x)	122 (10.6%)	130 (11.7%)
Sample deviation (σ)	159 m	147 m

circle and provides a baseline for the comparison of radar and rawinsonde proxy BSLs.

For the matched extrema, the differences between the extrema altitudes from the mean proxy BSLs and the individual dropsondes were combined to find the total sample deviations ($\sigma_{\max}$ and $\sigma_{\min}$) for the maxima and minima using

$$\sigma = \left[\frac{1}{r-1}\sum_{d=1}^{34}\sum_{m=1}^{y}\sum_{n=1}^{x}(\overline{z}_{d,m} - z_{d,m,n})^2\right]^{1/2}, \quad (4)$$

where r is the total number of matched maxima or minima, $\overline{z}_{d,m}$ is the altitude of a maximum or minimum from the mth mean proxy BSL from dropsonde set d, and $z_{d,m,n}$ is the altitude of the maximum or minimum from dropsonde n that matches the mth proxy BSL in dropsonde set d. In cases where a mean proxy BSL encompassed more than one proxy BSL from the same dropsonde, only the nearest extremum were used in these calculations. The $\sigma_{\max}$ was 159 m for the RH maxima altitudes and $\sigma_{\min}$ was 147 m for the RH minima (Table 2). The statistics presented in Table 2 provide a quantitative baseline for evaluation of the relationship between the boundaries of radar BSLs and RH extrema.

c. *Comparison of sounding RH extrema with radar BSLs*

A 3-h window of radar data centered at the sounding start time was used to compare each sounding-determined proxy BSL with a radar BSL. The 3-h time window corresponds to the time an air parcel traveling horizontally at 5.5–8.0 m s^{-1} (typical trade wind speeds during RICO; see Part I) would traverse across the radar analysis domain used in this study (60–90 km). The mean altitudes of the radar BSL boundaries within the time windows were determined by grouping points denoting BSL tops (or bases) and then calculating the average altitude of each top or base from each group of points. These mean altitudes were compared with the altitudes of the proxy BSLs from the rawinsondes. By using a 3-h window, we ensured that the sounding passed through the same region of space that was used to determine the radar BSLs. BSLs were determined from partial radar data if radar data were only available in part of the time window. If a BSL was detectable for only a portion of the 3-h time window, it was still used for this comparison. The impact of these choices on the comparison is discussed below in the context of Fig. 18.

The sounding analysis used for the BSL–proxy BSL comparison is identical to that used for the dropsonde intercomparison. For a proxy BSL to be matched with a mean radar BSL, we again required that at least 50% of the depth of one BSL be coincident in altitude with that of the other. Figure 18 summarizes the results. The results of the comparison depended on the number of estimates of a radar BSL boundary available in a 3-h window. If 100 or more estimates for both edges of a radar BSL were available, 64.3% of the radar BSLs matched proxy rawinsonde BSLs (Fig. 18a). If 50 or more estimates for both edges of a radar BSL were available, 60.1% matched (Fig. 18b). For all radar BSLs, regardless of the number of points available, 56.4% matched (Fig. 18c). The 64.3% match rate for the well-defined, 100+ point radar BSLs and rawinsonde proxy BSLs is remarkably close to the dropsonde proxy BSL ''self-agreement'' of 66.6%, providing strong evidence that the relationship is valid and that radar BSL boundaries can be used to track the evolution of the RH field, specifically RH maxima and minima.

We next determined to what degree the coincidence statistics were affected by variability in the radar BSL-top and-base estimates. Thus coincidence statistics were further broken down into subcategories by $\overline{\sigma} = (1/2)(\sigma_{\text{top}} + \sigma_{\text{bottom}})$, where σ_{top} and σ_{bottom} are the sample deviations of the radar BSL-top (e.g., coherent lines of red dots in Figs. 4–6) and -bottom (coherent lines of blue dots) edge estimates, binned in 50-m increments. In all three radar BSL categorizations (100+, 50+, and all estimates), no clear relationship was evident between $\overline{\sigma}$ and the number of BSL–proxy BSL matches. This suggests that the percentage of matches is not sensitive to the vertical spread of the points defining a BSL within a 3-h window, and thus noisier radar datasets that still have coherent BSLs are just as reliable as less-noisy radar datasets with sharply defined BSLs.

We also compared the altitudes of RH maxima and minima bounding the rawinsonde proxy BSLs with the radar-mean BSL boundaries. We applied the same criteria for matched, unmatched, and mismatched levels that was used in the dropsonde analysis (i.e., Fig. 16), with one exception. The dropsonde and rawinsonde proxy BSLs occurred at specific altitudes. The radar

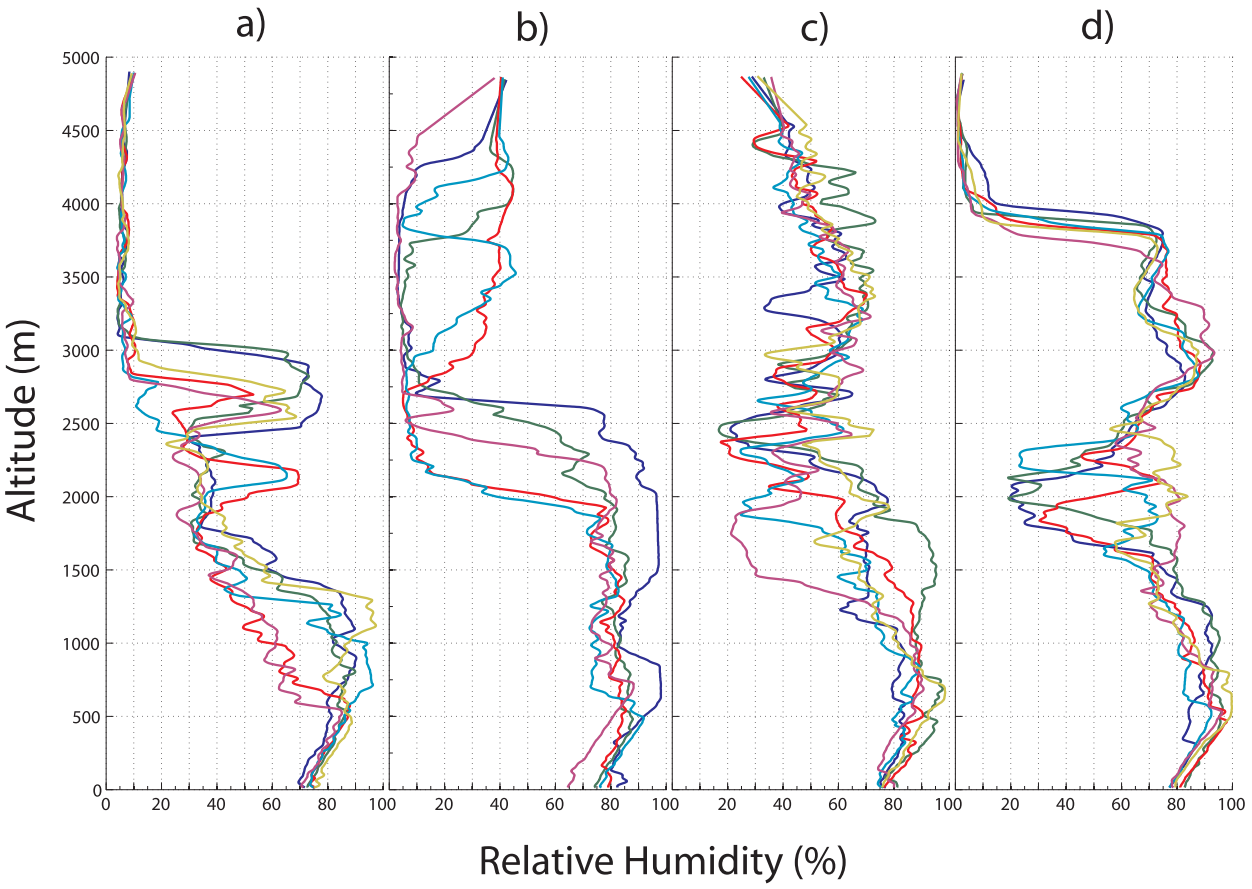

FIG. 17. RH profiles for 4 of the 34 sets of dropsondes used to establish the variability of the moisture field. Each dropsonde set was released along a 60-km-diameter circle within 25 min (Fig. 2). The sets shown are from (a) research flight (RF) 1, circle 1 (7 Dec 2004); (b) RF 10, circle 2 (5 Jan 2005); (c) RF 13, circle 2 (12 Jan 2005); and (d) RF 19, circle 1 (24 Jan 2005).

BSL boundaries are spatially averaged estimates that occur over a range of altitudes during a 3-h time period (e.g., the spread of dots on a single BSL edge in Figs. 4–6). For the radar BSLs, we asked 1) if a mean BSL boundary matched an appropriate rawinsonde RH extremum and 2) whether the appropriate rawinsonde extremum fell within the range of altitudes defining the radar BSL edge. Table 3 summarizes the statistics for the BSL boundaries. For the mean radar BSLs, approximately 48% (44%) of the bases (tops) matched. If we consider the range of radar BSL altitudes within the 3-h windows, 58% (55%) of the boundaries matched. The expected percentage of matches based on the dropsonde self-agreement analysis was about 60%. The statistics for the unmatched and mismatched BSL boundaries were also comparable to the statistics from the dropsonde analysis.

d. Summary

The data analysis presented above was used to test the idea that a radar BSL will exist in the interface layer between low-RH air overlying high-RH air, and that a layer not satisfying these conditions would be unlikely to support detectable Bragg scattering. The base of a BSL was assumed to coincide with an RH maximum and the top with an RH minimum. Given 1) the high level of spatial and temporal variability in the RH profile demonstrated by the dropsonde BSL self-agreement tests, 2) the difficulty in comparing point-measurement profiles from rawinsondes to large areal- and temporal-averaged profiles from radar, 3) the stringency of the criteria used for categorization of a match between the data from these instruments, and 4) the similar statistics generated in the dropsonde self-comparisons and the radar–rawinsonde comparisons, we conclude that the analyses presented support the relationship between BSL boundaries and RH maxima and minima. Despite the local variability in the moisture field illustrated by the dropsondes, the analyses above demonstrate that moisture layers in the TMBL can be tracked using Bragg scattering from an S-band radar, and that the layers can be used to investigate and understand the mesoscale structure and evolution of the TMBL, which is the subject of Part III.

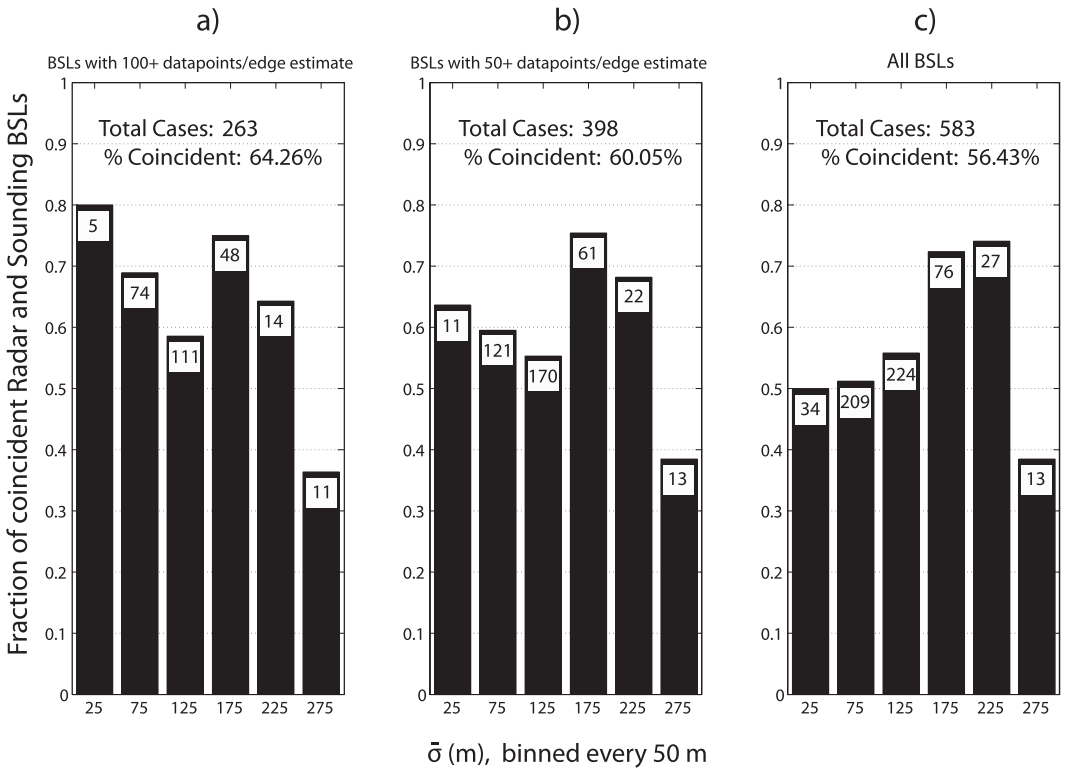

FIG. 18. Fraction of radar BSLs that have a matching proxy BSL in the corresponding sounding, binned by 50-m increments of $\overline{\sigma}$. The $\overline{\sigma}$ labels correspond to the bins' centers. The number of radar BSLs that fall into each bin category is shown at the top of each column in the histograms. The three different histograms show the statistics for (a) radar BSLs that have at least 100 estimates per edge, (b) radar BSLs that have at least 50 estimates per edge, and (c) all radar BSLs, regardless of the number of estimates available. The total number of radar BSLs in each category as well as the total percentage coincident rate are shown at the top of each histogram.

8. Conclusions

During the Rain in Cumulus over the Ocean (RICO) field campaign, persistent layers of enhanced equivalent radar reflectivity and reduced spectral width were observed in cloud-free regions of the tropical marine boundary layer with the S-Pol 10-cm-wavelength radar. We introduced a technique based on the Haar wavelet to identify layer edges using data collected while scanning in PPI mode. Advantages of this technique include near ''real time'' processing capability, high temporal resolution, and an independent estimate for each elevation angle scanned in a PPI volume. We used this technique to determine the mean layer boundary locations for individual radar scans, and constructed time–height diagrams of the layer boundaries. With these diagrams, we demonstrated that the layers are persistent, coherent features of the tropical marine boundary layer that delineate aspects of its mesoscale structure. We presented analyses and conceptual arguments exploring the nature of these layers—specifically, the primary scattering mechanism responsible for their existence, potential mechanisms for how they form and are sustained, and the relationship between the boundaries of the layers and the RH field. The following conclusions can be drawn about the nature of these layers:

1) The primary scattering mechanism producing the layers is Bragg scattering. Rayleigh reflectivity values calculated from haze particle size distributions from 14 RICO flights were much lower and statistically distinct from the radar reflectivities observed by S-Pol in clear-air regions of the tropical marine boundary layer. Since insect and bird echoes were not responsible for the layers, Bragg scattering appears to be the only viable mechanism to explain the layers' existence.
2) Two mechanisms were described that could create the large vertical gradients of radio refractivity N required for sustained Bragg scattering. The first involved turbulent mixing within a layer. It was argued that strong vertical gradients of N would develop at the top and bottom of a well-mixed turbulent layer and that the large vertical gradients of N would coincide with large vertical gradients of RH. The second mechanism was associated with

TABLE 3. Radar BSL–sounding comparison.

Layer comparison			
	All BSLs	50+ data points	100+ data points
Total layers	583	398	263
Matched layers (M)	329 (56.4%)	239 (60.0%)	169 (64.3%)
Unmatched layers (U)	254 (43.6%)	159 (40.0%)	94 (35.7%)

Extrema comparison		
	BSL base	BSL top
Total possible matches	583	583
Matched (m)	Mean: 282 (48.4%)	Mean: 258 (44.3%)
	Range: 340 (58.3%)	Range: 322 (55.2%)
Unmatched (u)	185 (31.7%)	185 (31.7%)
Mismatched (x)	58 (10.0%)	76 (13.1%)
Sample deviation (σ)	171 m	154 m

detrainment and evaporation of cloudy air near the bases of stable layers. As with the turbulence mechanism, large vertical gradients of N would coincide with large vertical gradients of RH.

3) The upper and lower boundaries of Bragg scattering layers (BSLs) were shown to occur near local minima and maxima, respectively, in the vertical RH profile. This conclusion was arrived at by first deriving an equation for the vertical gradient of N in terms of pressure, temperature, and RH and performing a scale analysis of the equation using the Barbuda-launched rawinsondes. The analysis showed that the RH vertical gradient term was the dominant factor contributing to large vertical gradients of N. We next compared the BSL boundaries to the RH profiles from Barbuda-launched soundings. To perform a meaningful comparison, we first established what constitutes significant RH extrema in the soundings that might provide the bounds for a BSL detectable by the radar, and how well RH measurements from a single sounding represent the moisture field in the ambient environment near the radar. A modified version of the Haar wavelet edge-finding technique was applied to the soundings to determine ''proxy BSLs.'' Dropsonde self-agreement tests, used to quantify the ambient environmental variability in RH, suggested that we should expect radar BSLs to agree with proxy rawinsonde BSLs 67% of the time. The actual agreement between radar and proxy rawinsonde BSLs was 64% when there were at least 100 estimates for radar BSL edges within a 3-h window centered on the rawinsonde launch time. The agreement between these statistics and the scale analysis of (3) together provide strong evidence that the relationship between BSL boundaries and RH maxima and minima exists and that radar BSL boundaries can be used to track the evolution of the RH field, specifically RH maxima and minima.

The results of this study illustrate two additional points: 1) The spatial and temporal variability of the RH profile in the tropical marine boundary layer is sufficiently large that a single rawinsonde profile is unlikely to represent the mean state of the moisture field within a 60-km-diameter circle centered on the rawinsonde site. This finding raises an issue of the representativeness of soundings launched at the typical low temporal and spatial resolution in many tropical studies (see also Part I). 2) The larger-scale RH field (tens of kilometers, characterized by the radar domain) can exhibit temporal coherence over time scales of hours to a day or more. These two points together imply that the BSLs reflect the mesoscale average of the small-scale moisture variability.

The radar analyses presented herein provide a new tool to refine and improve our understanding of the tropical marine boundary layer and to validate large-eddy simulation models. In Part III, we will use the BSL data to provide a statistical characterization and a revised conceptual model of the tropical marine boundary layer during RICO.

Acknowledgments. We would like to acknowledge the contributions of Francina Dominguez and Praveen Kumar to our understanding of wavelets. We thank Guangyu Zhao for providing Fig. 3. We also thank Charles Knight, Tammy Weckwerth, and an anonymous reviewer for their constructive comments. We especially thank the NCAR Earth Observing Laboratory RICO scientists and staff for their efforts in the field. Finally, thanks to the University of Louisville Department of Physics and Astronomy for hosting the lead author during a portion of this work. This research was supported by the National

Science Foundation (NSF) under Grants ATM-03-46172 and ATM-08-54954. Additional facilities support at the University of Louisville was provided by DOE Grant DE-SC0005473. Any opinions, findings and conclusions or recommendations expressed in this publication are those of the authors and do not necessarily reflect the views of NSF or DOE.

APPENDIX

Wavelet Analysis

For this analysis, the Haar father and mother wavelets, W_f and W_m, respectively, are

$$W_f(a,b) = a^{-1/2}\int_{r_1}^{r_n} f(r)\phi\left(\frac{r-b}{a}\right)dr$$

$$\approx a^{-1/2}\sum_{r_1}^{r_n} f(r)\phi\left(\frac{r-b}{a}\right)\Delta r,$$

$$\text{where } \phi\left(\frac{r-b}{a}\right) = \begin{cases} 1: & b-\frac{a}{2} \le r \le b+\frac{a}{2} \\ 0: & \text{elsewhere} \end{cases}, \quad \text{(A1)}$$

$$W_m(a,b) = a^{-1/2}\int_{r_1}^{r_n} f(r)h\left(\frac{r-b}{a}\right)dr$$

$$\approx a^{-1/2}\sum_{r_1}^{r_n} f(r)h\left(\frac{r-b}{a}\right)\Delta r,$$

$$\text{where } h\left(\frac{r-b}{a}\right) = \begin{cases} 1: & b-\frac{a}{2} \le r \le b \\ -1: & b \le r \le b+\frac{a}{2} \\ 0: & \text{elsewhere} \end{cases}, \quad \text{(A2)}$$

where a is the dilation or scale parameter, b is the translation, and n is the number of points in the dataset $f(r)$, where $f(r)$ is the data vector and r is an index specifying the position in the data vector. For example, for the first iteration of W_f, $f(r)$ is a set of spectral width values along one beam of radar data, and r is the range gate number. Unlike other wavelets, the first iteration of the Haar father (mother) wavelet is proportional to the averages (first derivatives or slopes) of adjacent paired points in $f(r)$ when using $a = 2$ data points. When using $a = 2$, r_1 and r_n are consecutive data points. Referring to Fig. A1a, four successive iterations of W_f were performed starting with the original data. A single iteration of W_m was performed on both the third and fourth W_f, yielding W_{m4} and W_{m5}, the fourth and fifth mother wavelets, respectively (the reason for calculation of both W_{m4} and W_{m5} is discussed in section 5). The calculation of W_{m4} (W_{m5}) was repeated 16 (32) times starting from the original data (e.g., Figs. A2a,b), except that the jth calculation started with index j along $f(r)$ (Fig. A1b). The union of the 16 W_{m4} results produced $g_4(r)$, a new scaled, smoothed, and shortened version of the first derivatives of the original data (e.g., Figs. A1b and A2c). Likewise, the union of the 32 W_{m5} results produced $g_5(r)$. The $g_4(r)$ and $g_5(r)$ data were then truncated at 528 and 512 data points, respectively. These correspond to radar ranges of 80.3 and 79.1 km. At an elevation angle of 5°, these ranges correspond to beam altitudes of 7.4 and 7.3 km.

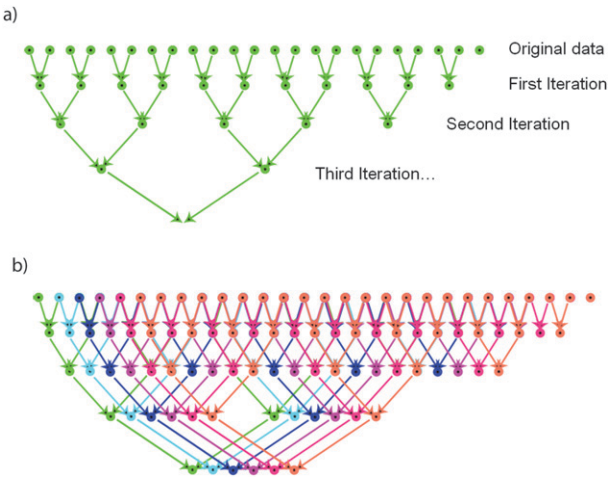

FIG. A1. Data analysis schematic detailing (a) successive wavelet iterations performed using a single starting point and (b) the union of these wavelet results from analysis carried out at successive starting points (each represented by a different color).

The final $g_4(r)$ for all beams in a PPI scan were averaged together to produce $\overline{g}_4(r)$ (Fig. A2d). Similarly, the final $g_5(r)$ were averaged together to produce $\overline{g}_5(r)$. Extrema in each $g(r)$ are located at the inflection points in $f(r)$, which correspond to the tops and bases of BSLs sampled by a single radar beam. Therefore, extrema in $\overline{g}(r)$ represent the average locations of the BSL bases and tops for a given radar scan. Extrema were identified as any maximum or minimum in $\overline{g}(r)$ that exceeded a threshold of 0.075 (0.50) m s^{-1} for W_{m4} (W_{m5}) (e.g., blue and red lines in Fig. A2). These thresholds were determined by experimentation to visually match the ring pattern in the original data. Note in Fig. A2d that the blue line at range gate 155 appears to be at a minimum. It is, in fact, a maximum, with adjacent minima on either side that did not exceed the thresholds. The 4/3 effective Earth's radius model using the spherical Earth

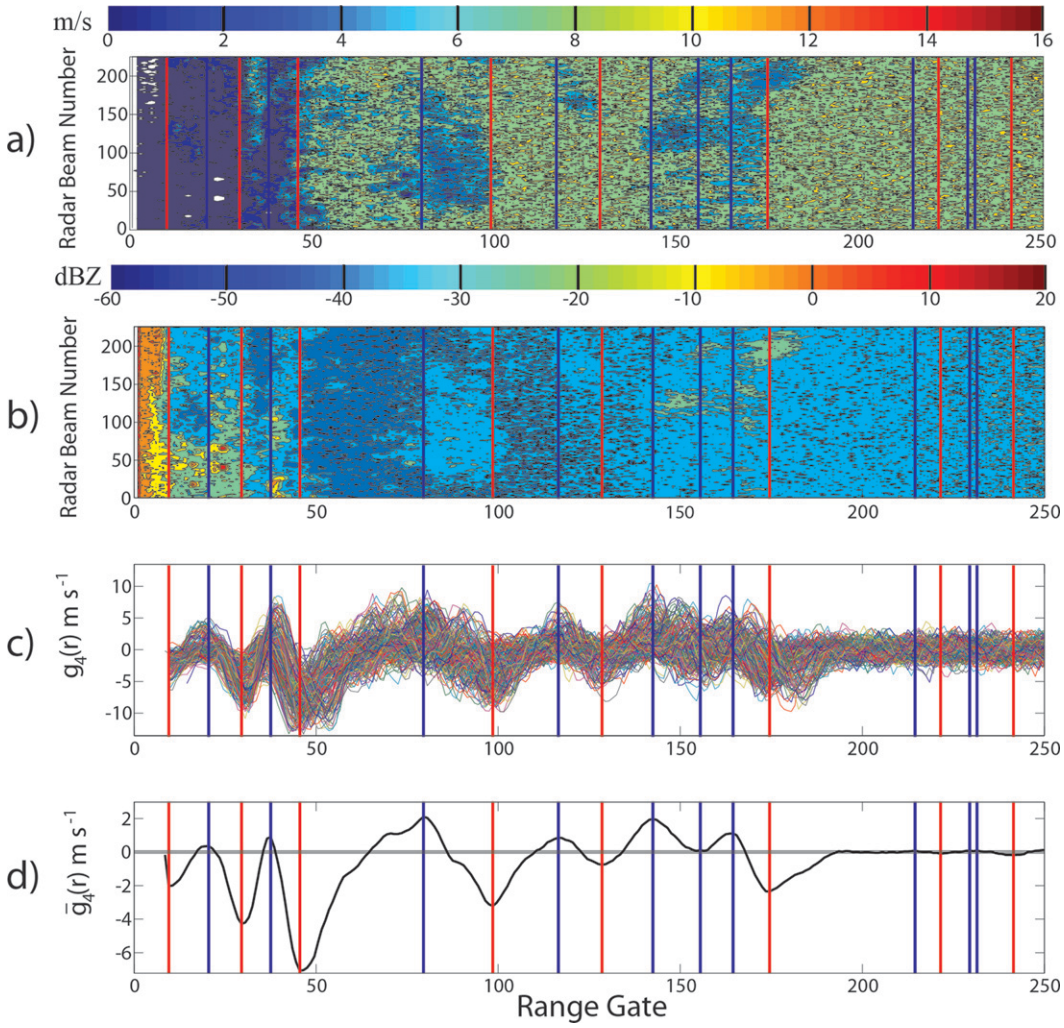

FIG. A2. Sample wavelet analysis. (a) The original spectral width measurements color contoured every 2 m s^{-1} and (b) the equivalent radar reflectivity factor measurements color contoured every 10 dBZ mapped onto Cartesian grids of range gate vs radar beam. (c) Each line represents $g_4(r)$ determined from the union of the 16 W_{m4} results for an individual beam of spectral width data. The $g_4(r)$ results from each beam in (a) are shown. (d) The average result, $\bar{g}_4(r)$, for the entire scan with thresholds (very near zero line) and local maxima (blue) and minima (red) shown. The first minimum is due to the island's eastern ridge (Fig. 2). The second minimum is the top of the transition layer. Noisy indicators are seen at the highest range gates. Layer edges in all panels are marked based on (d).

parabolic approximation was used for beam height calculations (e.g., Bean and Dutton 1968; Murrow 1990).

REFERENCES

Bean, B. R., and E. J. Dutton, 1968: *Radio Meteorology.* Dover Publications, 435 pp.

Chadwick, R. B., and E. E. Gossard, 1986: Radar probing and measurement of the planetary boundary layer: Part I Scattering from refractive index irregularities. *Probing the Atmospheric Boundary Layer,* D. H. Lenschow, Ed., Amer. Meteor. Soc., 163–182.

Davison, J. L., R. M. Rauber, L. Di Girolamo, and M. A. LeMone, 2013a: A revised conceptual model of the tropical marine boundary layer. Part I: Statistical characterization of the variability inherent in the wintertime trade wind regime over the western tropical Atlantic. *J. Atmos. Sci.,* **70,** 3005–3024.

——, ——, ——, and ——, 2013b: A revised conceptual model of the tropical marine boundary layer. Part III: Bragg scattering layer statistical properties. *J. Atmos. Sci.,* **70,** 3047–3062.

Doviak, R. J., and D. S. Zrnić, 1984: *Doppler Radar and Weather Observations.* Academic Press, 458 pp.

Ellis, S. M., and J. Vivekanandan, 2010: Water vapor estimates using simultaneous dual-wavelength radar observations. *Radio Sci.,* **45,** RS5002, doi:10.1029/2009RS004280.

Fabry, F., C. Frush, I. Zawadzki, and A. Kilambi, 1997: On the extraction of near-surface index of refraction using radar phase measurements from ground targets. *J. Atmos. Oceanic Technol.,* **14,** 978–987.

Gossard, E. E., R. B. Chadwick, W. D. Neff, and K. P. Moran, 1982: The use of ground-based Doppler radars to measure gradients,

fluxes, and structure parameters in elevated layers. *J. Appl. Meteor.,* **21,** 211–226.

——, ——, T. R. Detman, and J. Gaynor, 1984a: Capability of surface-based clear-air Doppler radar for monitoring meteorological structure of elevated layers. *J. Climate Appl. Meteor.,* **23,** 474–485.

——, W. D. Neff, R. J. Zamora, and J. E. Gaynor, 1984b: The fine structure of elevated refractive layers: Implications for the over-the-horizon propagation and radar sounding systems. *Radio Sci.,* **19,** 1523–1533.

——, J. E. Gaynor, R. J. Zamora, and W. D. Neff, 1985: Fine-structure of elevated stable layers observed by sounder and *in situ* tower sensors. *J. Atmos. Sci.,* **42,** 2156–2169.

Heinselman, P. L., D. J. Stensrud, R. M. Hluchan, P. L. Spencer, P. C. Burke, and K. L. Elmore, 2009: Radar reflectivity-based estimates of mixed layer depth. *J. Atmos. Oceanic Technol.,* **26,** 229–239.

Knight, C. A., and L. J. Miller, 1993: First radar echoes from cumulus clouds. *Bull. Amer. Meteor. Soc.,* **74,** 179–188.

——, and ——, 1998: Early radar echoes from small, warm cumulus: Bragg and hydrometeor scattering. *J. Atmos. Sci.,* **55,** 2974–2992.

Kumar, P., and E. Foufoula-Georgiou, 1997: Wavelet analysis for geophysical applications. *Rev. Geophys.,* **35,** 385–412.

Loehrer, S. M., T. A. Edmands, and J. A. Moore, 1996: TOGA COARE upper-air sounding data archive: Development and quality control procedures. *Bull. Amer. Meteor. Soc.,* **77,** 2651–2671.

——, S. F. Williams, and J. A. Moore, 1998: Results from UCAR/JOSS quality control of atmospheric soundings from field projects. Preprints, *10th Symp. on Meteorological Observations and Instrumentation,* Phoenix, AZ, Amer. Meteor. Soc., 1–6.

Luers, J. K., 1997: Temperature error of the Vaisala RS90 radiosonde. *J. Atmos. Oceanic Technol.,* **14,** 1520–1532.

Murrow, D. J., 1990: Height finding and 3D radar. *Radar Handbook,* M. I. Skolnik, Ed., McGraw-Hill, 20.1–20.40.

Ottersten, H., 1969: Atmospheric structure and radar backscattering in clear air. *Radio Sci.,* **4,** 1179–1193.

Perry, K. D., and P. V. Hobbs, 1996: Influences of isolated cumulus clouds on the humidity of their surroundings. *J. Atmos. Sci.,* **53,** 159–174.

Rauber, R. M., and Coauthors, 2007: Rain in shallow cumulus over the ocean. *Bull. Amer. Meteor. Soc.,* **88,** 1912–1928.

——, G. Zhao, L. Di Girolamo, and M. Colón-Robles, 2013: Aerosol size distribution, particle concentration, and optical property variability near Caribbean trade cumulus clouds: Isolating effects of vertical transport and cloud processing from humidification using aircraft measurements. *J. Atmos. Sci.,* **70,** 3063–3083.

Roberts, R. D., and Coauthors, 2008: REFRACTT 2006. *Bull. Amer. Meteor. Soc.,* **89,** 1535–1548.

Snider, J. R., and M. D. Petters, 2008: Optical particle counter measurement of marine aerosol hygroscopic growth. *Atmos. Chem. Phys.,* **8,** 1949–1962.

Snodgrass, E. R., L. Di Girolamo, and R. M. Rauber, 2009: Precipitation characteristics of trade wind clouds during RICO derived from radar, satellite, and aircraft measurements. *J. Appl. Meteor. Climatol.,* **48,** 464–483.

Strapp, J. W., W. R. Leaitch, and P. S. K. Liu, 1992: Hydrated and dried aerosol-size-distribution measurements from Particle Measuring Systems FSSP-300 probe and deiced PCASP-100X probe. *J. Atmos. Oceanic Technol.,* **9,** 548–555.

Tatarski, V. I., 1961: *Wave Propagation in a Turbulent Medium.* McGraw-Hill, 285 pp.

Verver, G., M. Fujiwara, P. Dolmans, C. Becker, P. Fortuin, and L. Miloshevich, 2006: Performance of the Vaisala RS80A/H and RS90 Humicap sensors and the Meteolabor "Snow White" chilled-mirror hygrometer in Paramaribo, Suriname. *J. Atmos. Oceanic Technol.,* **23,** 1506–1518.

Zhao, G., and L. Di Girolamo, 2007: Statistics on the macrophysical properties of trade wind cumuli over the tropical western Atlantic. *J. Geophys. Res.,* **112,** D10204, doi:10.1029/2006JD007371.